Published online 10 February 2022

Nucleic Acids Research, 2022, Vol. 50, No. 19 ***10801–10816***
https://doi.org/10.1093/nar/gkac059

NAR Breakthrough Article

RbgA ensures the correct timing in the maturation of the 50S subunits functional sites

Amal Seffouh[1,2], Chirstian Trahan[3], Tanzila Wasi[1,2], Nikhil Jain[4,5], Kaustuv Basu[1,2], Robert A. Britton[4,5], Marlene Oeffinger[3,6,7] and Joaquin Ortega[1,2,*]

[1]Department of Anatomy and Cell Biology, McGill University, Montreal, Quebec H3A 0C7, Canada, [2]Centre for Structural Biology, McGill University, Montreal, Quebec H3G 0B1, Canada, [3]Center for genetic and neurological diseases, Institut de Recherches Cliniques de Montréal (IRCM), Montréal, Quebec H2W 1R7, Canada, [4]Department of Molecular Virology and Microbiology, Baylor College of Medicine, Houston, TX 77030, USA, [5]Center for Metagenomics and Microbiome Research, Baylor College of Medicine, Houston, TX 77030, USA, [6]Département de Biochimie et Médecine Moléculaire, Université de Montréal, Montréal, Quebec H3T 1J4, Canada and [7]Division of Experimental Medicine, McGill University, Montréal, Quebec H4A 3J1, Canada

Received September 26, 2021; Revised January 15, 2022; Editorial Decision January 17, 2022; Accepted January 26, 2022

ABSTRACT

RbgA is an essential protein for the assembly of the 50S subunit in *Bacillus subtilis*. Depletion of RbgA leads to the accumulation of the 45S intermediate. A strain expressing a RbgA variant with reduced GTPase activity generates spontaneous suppressor mutations in uL6. Each suppressor strain accumulates a unique 44S intermediate. We reasoned that characterizing the structure of these mutant 44S intermediates may explain why RbgA is required to catalyze the folding of the 50S functional sites. We found that in the 44S particles, rRNA helices H42 and H97, near the binding site of uL6, adopt a flexible conformation and allow the central protuberance and functional sites in the mutant 44S particles to mature in any order. Instead, the wild-type 45S particles exhibit a stable H42-H97 interaction and their functional sites always mature last. The dependence on RbgA was also less pronounced in the 44S particles. We concluded that the binding of uL6 pauses the maturation of the functional sites, but the central protuberance continues to fold. RbgA exclusively binds intermediates with a formed central protuberance and licenses the folding of the functional sites. Through this mechanism, RbgA ensures that the functional sites of the 50S mature last.

GRAPHICAL ABSTRACT

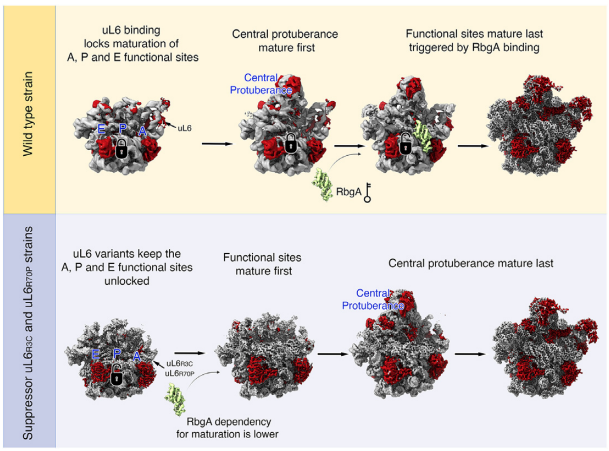

INTRODUCTION

Ribosome biogenesis GTPase A (RbgA) is an essential protein for assembling the 50S subunit in *Bacillus subtilis* (1,2). RbgA is widely distributed in the genomes of Gram-positive and some Gram-negative bacteria, including important human pathogens such as *Streptococcus pneumoniae*, *Staphylococcus aureus*, *Vibrio cholerae* and *Neisseria meningiditis*. Still, RbgA is absent in *Escherichia coli*, the model system used to study Gram-negative bacteria.

B. subtilis cells depleted of RbgA accumulate an assembly intermediate called $45S_{RbgA}$. Analysis of these particles provided the first insights on how RbgA assists the late stages of assembly of the 50S subunit (3,4). They revealed that the

*To whom correspondence should be addressed to Joaquin Ortega. Tel: +1 514 398 5230; Email: joaquin.ortega@mcgill.ca

function of RbgA is central to the maturation of the A, P and E functional sites. Upon binding to the P-site, RbgA induces rRNA helices H91-92 and H38 in the A site and H93 in the P site to adopt their mature conformation. RbgA binding also has an overall stabilizing effect in the ribosomal protein (r-protein) uL6 and H80-88, forming the central protuberance (CP) (5).

Additional maturation steps are still required beyond those induced by RbgA for the assembling subunit to reach the mature state. These include stabilizing the long helix H68 in the E site, H89 in the A site and folding of H69 and H71 in the P site. Other assembly factors, including YphC and YsxC, along with several r-proteins (uL16, bL27, bL28, bL33, bL35 and bL36) (6) bind to the assembling subunit at these late maturation stages and contribute to catalyze these rearrangements (7). Entry of r-protein uL16 is one of the last maturation events and has a significant effect on the placement of the rRNA helices forming the functional sites (4,8,9). Conformational changes catalyzed by the entry of uL16 trigger the RbgA GTPase activity and subsequent release of RbgA (4). All these combined conformational changes finally transition the assembling particle into the mature 50S subunit.

The $45S_{RbgA}$ particles accumulating in RbgA depleted cells mature *in vivo* and are integrated into complete functional ribosomes (4). However, the available cryo-EM structures of the $45S_{RbgA}$ particle alone (3,4) and in complex with RbgA (5) do not reveal why the $45S_{RbgA}$ particle is entirely dependent on RbgA to complete the maturation process. A genetic study suggesting a functional interaction between RbgA and r-protein uL6 (10) provided the first hint. A single point mutation from Phe 6 to Ala in RbgA (RbgA-F6A) significantly reduces RbgA GTPase activity and causes the strain to exhibit a slow growth phenotype and accumulate $45S_{RbgA}$ particles. Spontaneous suppressor mutants of RbgA-F6A were isolated, and each suppressor strain bore a single point mutation in the *rplF* gene (encoding for r-protein uL6). All suppressor strains had a significantly faster growth rate (46–77 min) than the strain expressing RbgA-F6A (173 min) (10). They also accumulated novel 44S ribosomal particles that were able to complete their maturation and evolve into functional 50S subunits in the presence of the functionally compromised RbgA-F6A variant.

In our study, we inquired why the $45S_{RbgA}$ particle is entirely dependent on RbgA for completion of the maturation process, whereas the 44S particles can mature in the presence of a functionally compromised RbgA variant. To this end, we purified 44S particles from the R3C ($44S_{R3C}$) and R70P ($44S_{R70P}$) RbgA-F6A suppressor strains. These strains express uL6 either with an Arginine 3 to Cysteine (R3C) or an Arginine 70 to Proline (R70P) single point mutations (10). Cryo-electron microscopy (cryo-EM) analysis showed that the presence of uL6 variants in the 44S particles caused rRNA helices H97 and H42, near the binding site of uL6 to adopt a flexible conformation. Instead, in the mature 50S subunit and $45S_{RbgA}$ particles, with normal uL6 content, H97 interacts with H42 adopting their native conformation and forming the structural motif that supports the GTPase associated center (GAC). This allowed the 44S particles to keep a less stringent assembly program and the maturation of the functional sites can occur before or after the central protuberance (CP). In addition, the $44S_{R70P}$ particles matured in a reaction where RbgA was no added.

These experiments indicate that the assembly intermediate represented by the $45S_{RbgA}$ particle constitutes a critical step on the 50S assembly, and the essential role of RbgA is to unlock the conformation adopted by H97 and H42, which is imposed by the entry of uL6. RbgA only binds to $45S_{RbgA}$ particles with a fully assembled CP (5) and licenses further folding of the functional core of the subunit. By this mechanism, RbgA ensures the maturation of the functional sites occurs last and only after the CP has been formed.

MATERIALS AND METHODS

Bacterial strains

The $45S_{RbgA}$ particles used as control were purified from the RbgA-depleted *B. subtilis* strain (RB301), containing the *ylqF* gene (encoding RbgA) under the control of an isopropyl-β-D-thiogalactopyranoside (IPTG) inducible P_{spank} promotor. The construction of this strain has been described somewhere else (2).

The $44S_{R3C}$ and $44S_{R70P}$ particles were obtained from *B. subtilis* suppressor strains RB1055 and RB1051. The construction of these strains was described previously (10). Both strains contain a *rbgA*-F6A mutant gene as the only copy of *rbgA* in the cell. In addition, RB1055 has an R3C single point mutation in the gene encoding r-protein uL6 (*rplF*). In the case of RB1051, the mutation in uL6 is R70P.

The ^{15}N-labeled 70S ribosomes used as a reference for qMS were prepared from B. subtilis RB136 strain (WT-py79 prototrophic strains) (11).

Purification of ribosomal particles

The $44S_{R3C}$ and $44S_{R70P}$ particles were isolated from the RB1055 and RB1051 strains, respectively (10). We also obtained $70S_{R70P}$ ribosomes from the RB1051 strain. Strains were cultured on LB agar plates supplemented with 100 μg/ml of spectinomycin incubated at 37°C. Multiple individual colonies from each plate were resuspended in 1 ml of pre-warmed LB media. This suspension was used to inoculate 600 ml of pre-warmed LB medium supplemented with 100 μg/ml spectinomycin. Cultures were shaken at 250 rpm during incubation at 37°C. RB1055 and the RB1051 strains exhibited a doubling time of 69 ± 1 min and 46 ± 4 min, respectively. The culture was started at an A_{600} of 0.01 and harvested when A_{600} reached between 0.4 and 0.5.

The $45S_{RbgA}$ particles were isolated from the RB301 (2) after applying a RbgA depletion protocol. The strain was first grown at 37°C on LB plates supplemented with 5 μg/ml chloramphenicol and 1 mM IPTG. RbgA depletion was obtained by resuspending a few colonies from the plate in 100 ml of pre-warmed LB medium containing 5 μg/ml chloramphenicol (initial A_{600} around 0.01–0.02). The culture was then grown to A_{600} 0.4–0.5 at 37°C and used to inoculate 600 ml of fresh pre-warmed media. This new culture was incubated at 37°C with agitation. To prevent the generation of a genetic suppressor, the culture was harvested when cells reached a doubling time between 140 and 150 min, corresponding to A_{600} 0.3–0.4.

To obtain the ^{15}N-labeled 70S ribosomes, we grew *B. subtilis* RB136 strain (WT-py79 prototrophic strains) aerobically in 1 X MSpitzM9 medium containing 8 mM K_2HPO_4, 4.4 mM KH_2PO_4, 0.39 mM Na_3-citrate, 10 mM $MgCl_2$, 10 mM $MgSO_4$, 5.6 mM glucose, 50 μM Na_3·EDTA, 25 mM $CaCl_2$, 50 μM $FeCl_3$, 0.5 μM $ZnSO_4$, 0.5 μM $CuSO_4$, 0.5 μM $MnSO_4$, 0.5 μM $CoCl_2$, 0.04 μM d-biotin, 0.02 μM folic acid, 0.08 μM vitamin B1, 0.11 μM calcium pantothenate, 0.4 nM vitamin B12, 0.2 μM nicotinamide, 0.07 μM riboflavin and 7.6 mM ($^{15}NH_4)_2SO_4$). Cells in this media were incubated with agitation at 37°C and harvest when they grew to A_{600} ∼0.5.

The $44S_{R3C}$, $44S_{R70P}$, $45S_{RbgA}$ particles, $70S_{R70P}$ ribosomes and ^{15}N-labeled 70S ribosomes were purified using the same approach. Cells were harvested at the A_{600} indicated above by centrifugation at 3000 *g* for 20 min in a Beckman JLA-8.1000 rotor, and the obtained pellet was washed with 30 ml PBS buffer. The cell pellet was then resuspended in 8 ml of buffer A (20 mM Tris–HCl pH 7.5, 60 mM NH_4Cl, 10 mM Mg acetate, 0.5 mM EDTA, 3 mM β-mercaptoethanol, complete EDTA-free protease inhibitors (Roche), 50 μl RNase-free DNase (Roche) and 0.5% Tween-20). Cells were lysed by four consecutive passes through a French press set at 20 000 lbs/in^2. The cell lysate was then centrifuged at 32 000 *g* for 40 min in a MLA-80 rotor to clear cell debris. The clarified lysate was layered over a 1.1 M sucrose cushion of equal volume in buffer B (20 mM Tris–HCl at pH 7.5, 60 mM NH_4Cl, 10 mM Mg acetate, 0.5 mM EDTA, 3 mM β-mercaptoethanol) and centrifuged for 16 h at 110 000 *g* in a Beckman MLA- 80 rotor. The ribosomal pellet was washed by buffer C (20 mM Tris–HCl [pH 7.5], 60 mM NH_4Cl, 10 mM Mg acetate, 0.5 mM EDTA and 7 mM β-mercaptoethanol) under gentle agitation, before being pelleted again by centrifugation for 16 h at 110 000 *g* with the MLA-80 rotor. The ribosomal pellet was then resuspended in buffer E (10 mM Tris–HCl pH 7.5, 15 mM Mg acetate, 60 mM NH_4Cl, 3 mM β-mercaptoethanol). Approximately 300 A_{260} units of resuspended crude ribosomes were then loaded at the top of a 35 ml 18–43% (w/v) sucrose density gradients equilibrated in buffer E and centrifuged for 14 h at 60 000 *g* in a Beckman SW 32 Ti rotor. Gradients were then fractionated on an AKTAprime FPLC system (GE Healthcare Life Sciences) by monitoring UV absorbance at 254 nm. Fractions corresponding to ribosomal subunits of interest or 70S ribosomes were pooled and pelleted by centrifugation for 16 h at 110 000 *g* in a Beckman MLA-80 rotor. The ribosomal subunit and 70S ribosome pellets were solubilized in buffer E, quantified, frozen in liquid nitrogen and stored at −80°C.

Protein overexpression and purification

Overexpression of RbgA was obtained by transforming *Escherichia coli* BL21 (DE3) cells with pET21b-*ylqF* plasmid (2). Expression and subsequent purification of RbgA were done according to previously published protocols (5).

Purified RbgA F6A variant was obtained using the same expression system and purification approach as the wild-type RbgA protein, but after Phe 6 was replaced by Ala using the QuickChange IIXL kit (Stratagene) (12).

Quantitative mass spectrometry

Purified ribosome subunits were individually mixed in equimolar ratios (5 pmol each) with ^{15}N-labeled 70S purified ribosomes in a volume of 10 μl in buffer E. One volume of 8 M urea in 50 mM Tris–HCl, pH 8 was added to the samples, which were then reduced with 5 mM DTT (55 mM stock in 50 mM Tris–HCl pH 8 and 8 M urea) and then incubated for 30 min at 37°C in with gentle agitation (Thermomixer set at 350 RPM). Cysteines were then alkylated in 16 mM iodoacetamide (192 mM stock in 50 mM Tris, pH 8 and 8 M urea) by incubation at room temperature in the dark for an additional 30 min. Trypsin / Lys-C (V5073, Promega) was added at a 1:25 enzyme to protein ratio, and the Lys-C digestion was allowed to proceed for 4 h at 37°C with gentle agitation. Urea was finally diluted to 1 M using 50 mM Tris–HCl, pH 8 to will enable the trypsin digestion to proceed overnight. All agitations were done in a thermomixer at 350 RPM. The next day, trifluoroacetic acid (TFA) and acetonitrile (ACN) were added to final concentrations of 0.5% and 2%, respectively. The peptide samples were cleaned on Peptide Cleanup C18 Spin Tubes (Agilent, 5188–2750) as per manufacturer recommendations, except that peptides were eluted with 80% ACN containing 0.5% TFA. Eluted peptides were brought to dryness; then, they were resuspended in 34 μl of 2% ACN with 1% formic acid (FA) and an internal retention time (iRT) standard peptide mix (Biognosys, Ki-3002–1). Samples volumes corresponding to 1.4 μg each were injected in technical triplicates on a PicoFrit fused silica capillary column (15 cm × 75 μm i.d; New Objective), self-packed with C-18 reverse-phase resin (Jupiter 5 μm particles, 300 Å pore size; Phenomenex) using a high-pressure packing cell on the Easy-nLC II system (Proxeon Biosystems). Solvent A was 2% ACN with 1% FA, while solvent B was 99% ACN with 1% FA. Peptides were loaded on-column at a 600 nl/min flow rate and eluted over a 2-slope gradient at a 250 nl/min flow rate. Solvent B was increased from 2 to 45% over 120 min and from 45 to 85% over 10 min. The column was coupled to the Orbitrap Fusion (ThermoFisher Scientific) equipped with a Proxeon nanoelectrospray Flex ion source.

We employed a library-free WiSIM-DIA strategy to collect and analyze the data (Thermo Scientific). Full scans acquisitions (300–530, 530–760 and 760–990 m/z) were carried out in the Orbitrap at a resolution of 240 000. Each full scan was followed by 20 linear trap acquisition windows at 12 m/z increments, covering each full scan. Matching m/z window precursor ions were fragmented by HCD at a 30% collision energy. MS ion fill times and AGC targets were set to 50 ms and 3×10^4, and to 47 ms and 5×10^4 for MS2, respectively (13).

Raw files were analyzed by directDIA with Spectronaut v.13.12.200217.43655 (Biognosys) using a fasta library consisting of the large ribosomal subunit proteins of Bacillus subtilis strain 168, extracted from UP000001570.fasta (downloaded on 14 February 2020). Considered peptide length was 6–52 amino acids, with two miscleavages tolerance according to semi-specific Trypsin/P digestion rule. The data were extracted with both MS and MS2 tolerance levels set at dynamic with correction factors of 1 (default). Carbamidomethylation of cysteine was set as fixed mod-

ifications, while oxidation of methionine and protein N-termini acetylation were set as a variable. Machine learning across experiments was selected for proteins and precursors identification with both Qvalues cutoffs at 0.01. MS1 was set to a minimum of 3 interference-free precursors; MS2 was set to a minimum of 4 interference-free fragments. Quantification was made at the MS1 level by using median XIC areas on peptide precursors levels. Only proteotypic peptides meeting the Qvalue threshold were considered. MS1 XIC isotopic envelopes were visually inspected for manual approval or rejection. Across all runs, 105 precursors had a full profile, with 93 peptides matching to 28 proteins and groups. Globally, 8–9 data points were measured per peak, and data completeness was 98.5%. Median CVs for each sample group varied from 2.5 to 2.9%, with an overall average peak capacity of 319.1 (ranging from 315.4 to 324.9 for each conditions) and a median XIC width of 4 min across samples (ranging from 3.8 to 4.2 min per condition). The light to heavy precursors median raw intensity ratios were normalized on uL24 $^{14}N/^{15}N$ median ratio to obtain relative protein occupancies values for all triplicates, which were then plotted using ggplot2.

Microscale thermophoresis experiments

Affinity measurements using microscale thermophoresis (MST) were carried out with a Monolith NT.115 instrument (NanoTemper Technologies) using the experimental set up previously described (5).

In vitro maturation assays

The starting material for these experiments was the purified ribosomal particles from the RB1055 and RB1051 strains in buffer E before fractionating the various ribosomal particles using sucrose gradient centrifugation. Approximately 1.6 mg of total ribosomes were used per gradient. At the beginning of the maturation assay, the purified ribosomes were supplemented with either 2 mM GMPPNP or GTP as indicated and then kept at 4°C or incubated at 37°C for 15 min in the presence or absence of RbgA. In those experiments containing RbgA, the assembly factor was added to a 5-fold or 40-fold molar excess concentration with respect to the ribosomes, depending on the experiment. After incubation, the ribosomal mixture was loaded on top of 18–43% sucrose density gradients equilibrated in buffer E and centrifuged for 14 h at 60 000 *g* in a Beckman SW 32 Ti rotor. Gradients were then fractionated on a FPLC ÄKTA Basic (GE Healthcare Life Sciences) by monitoring UV absorbance at 254 nm.

Western blotting

Approximately 1 μM of the 50S, $45S_{RbgA}$, $44S_{R3C}$ and $44S_{R70P}$ of purified ribosomal particles were resolved by 12% SDS/12% PAGE and transferred according to manufacturer's protocols to a nitrocellulose membrane (Hybond ECL, GE Healthcare, Buckinghamshire, UK) by semi-dry transfer system (Bio-Rad trans-blot turbo transfer system 690BR). Three known amounts of purified RbgA (0.05, 0.1 and 0.5 μg) were also loaded on the gel as a positive control. The membrane was blocked with 5% skim milk in TBS-T buffer (50 mM Tris-HCl [pH 7.4], 150 mM NaCl, 0.1% Tween 20) for 2 h at room temperature. The membrane was incubated with a 1:1000 dilution of the anti-RbgA serum overnight at 4°C. It was washed three times for 10 min with TBS-T buffer and then incubated for 1 h with a 1:16 000 dilution of goat anti-rabbit polyclonal antibodies conjugated to peroxidase (Sigma). Finally, the membrane was washed three times for 10 min with TBS-T buffer. The filter was developed by using an enhanced chemiluminescence kit (ECL plus, GE Healthcare) in an imager system (ChemiDoc MP, Bio-Rad). The anti-RbgA serum was prepared by immunization of rabbits with C-terminal His-tagged RbgA protein.

Cryo-electron microscopy

To prepare the cryo-EM grids containing untreated $44S_{R3C}$ and $44S_{R70P}$ particles, purified particles were diluted in buffer E to a concentration of 160 and 200 nM, respectively. A volume of 3.6 μl of these dilutions was applied directly to the grid.

In the experiment to visualize the RbgA treated $44S_{R3C}$ and $44S_{R70P}$ particles, we assembled a reaction 10-fold concentrated with respect to the mixture applied to the grid. In the RbgA treated $44S_{R3C}$ particles, the concentrated reaction was assembled in 10 μl in buffer E containing 2 mM of GMPPNP and a concentration of 1.5 μM of $44S_{R3C}$ particles and a 40-fold excess of RbgA. The reaction containing the RbgA treated $44S_{R70}$ particles was assembled similarly, but the concentrated reaction contained 1.8 μM of $44S_{R70}$ particles. Both reactions were incubated at 37ºC for 15 min and then diluted 10-fold in buffer E containing 2 mM GMPPNP and 6 or 7.2 μM RbgA ($44S_{R3C}$ or $44S_{R70}$, respectively) before applying the mixture to the cryo-EM grid.

The sample containing the $44S_{R70}$ particles treated at 37 ºC for 15 min was prepared by preparing a 10 μl reaction in buffer E containing 2 mM GMPPNP and ribosomal particles at a concentration of 1.8 μM. The reaction was subjected to incubation and diluted 10-fold in the same buffer before applying 3.6 μl to the grid.

The sample to image $70S_{R70}$ ribosomes was produced by modifying the ribosome purification protocol described above. The lysate supernatant obtained from the RB1051 (R70P) strain in buffer A was supplemented with GMPPNP to a concentration of 2 mM and then kept at 4°C for 15 min before. The lysate supernatant was then loaded in an 18–43% sucrose density gradient equilibrated in buffer E and centrifuged for 14 h at 60 000 *g* in a Beckman SW 32 Ti rotor. The gradient was fractionated on a FPLC ÄKTA Basic (GE Healthcare Life Sciences) by monitoring UV absorbance at 254 nm. Fractions containing the $70S_{R70}$ ribosomes were pelleted by centrifugation, then solubilized diluted in buffer E. A volume of 3.6 μl of the $70S_{R70}$ ribosomes at a concentration of 180 nM was applied directly to the grid.

Cryo-EM grids (c-flat CF-2/2–2C-T) used for all samples were prepared by evaporating a continuous layer of carbon (5–10 nm) to reduce exposure of the ribosomal particles to the air-water interface. Right before applying the samples,

grids were washed in chloroform for 2 h and treated with glow discharged in air at 5 mA for 15 s. Next, grids were vitrified in liquid ethane using a Vitrobot Mark IV (Thermo Fisher Scientific Inc.) using one blotting time for 3 s and a blot force + 1. The Vitrobot chamber was set to 25 ºC and 100% relative humidity.

All datasets were collected at FEMR-McGill using a Titan Krios microscope at 300 kV equipped with a Gatan BioQuantum LS K3 direct electron detector. The software used for data collection was SerialEM (14). Images were collected in counting mode according to the parameters described in Supplementary Tables S2–S5.

Image processing

Cryo-EM movies were corrected for beam-induced motion using RELION's implementation of the MotionCor 2 algorithm (15,16). CTF parameter estimation was done using the Gctf program (17). The remaining processing steps were done using RELION-3 (16). Individual particles in the images were identified using auto-picking. These particles were extracted and subjected to one or more cycles of reference-free 2D classification to remove false positives from the auto picking process. Cleaned datasets were sent for a multi-layered 3D classification strategy described in detail for each sample in Supplementary Figures S2, S4, S8, S10, S15, S17 and S20. The initial 3D reference used for these classifications was either a 60 Å low pass filtered map of the mature 50S subunit from *B. subtilis* created from 3j9w.pdb (18) using the Xmipp program (19) or the intermediate cryo-EM maps obtained during classification. The 3D classifications did not used masks. To speed up the computer calculations, the 2D and 3D classifications were performed using particle images binned by 4. However, we use full-size images in the refinement steps. Particles assigned to maps representing the same conformation were pooled together and used for 3D auto-refine. The numbers of particles assigned to each class and included in each refinement are described in Supplementary Tables S2–S5. For all cryo-EM maps, refinement was performed in four stages: In the first stage, the 3D auto-refine was performed without a mask. The resulting map was used to create a mask and was also used as the initial reference for a second stage refinement that included one additional 3D auto-refine cycle. Masks were created with 'relion_mask_create' command extending the binary mask by four pixels and creating a soft edge with a width of four pixels. The initial threshold for binarization of the mask varied depending on the structure. In the third step, we used the output of the last 3D auto-refine job as the input for CTF refinement. In this process, we selected 'Estimate (anisotropic) magnification' as no, 'Perform CTF parameter fitting' as Yes and selected 'Fit defocus' as 'Per-particle' and 'Fit astigmatism as 'Per-micrograph.' We selected 'No' for 'Fit B-factor', 'Fit phase-shift', 'Estimate trefoil' and 'Estimate 4th order aberrations'. However, we selected 'Yes' for 'Estimate beam tilt, as our data were collected using this approach. In the fourth step, we used the output from the CTF refinement job to perform Bayesian polishing to correct for per-particle beam-induced motion before subjecting these particles to the last cycle of 3D auto-refine. Bayesian polishing was performed using sigma values of 0.2, 5000 and 2 for velocity, divergence and acceleration, respectively. Sharpening of the final cryo-EM maps was done with RELION (16). Because sharpening causes fragmentation of densities in regions affected by flexibility, including the rRNA H42-44 of interest here, the comparisons in our study were all performed with unsharpened maps. The average resolution for the obtained cryo-EM structures was estimated by gold-standard Fourier shell correlation. Resolution estimation is reported using a FSC threshold value of 0.143. Local resolution analysis was done with RELION (16). Cryo-EM map visualization was done by UCSF Chimera (20) and Chimera X (21,22).

Molecular model building

To build the molecular models for the $44S_{R3C}$ class 1 and $44S_{R70P}$ class 1 that were used to calculate the temperature maps shown in Supplementary Figure S7, we first used the Chimera program (20) to fit by rigid-body docking the atomic model of the mature 50S subunit from *B. subtilis* (PDB ID: 3j9w) (18) into the cryo-EM density maps. These initial models were improved by rounds of real-space refinement in Phenix (23) and manual model building in Coot (24,25). The connectivity of the cryo-EM maps was improved using the automatic sharpening tool phenix.auto_sharpen (26), which is available as part of the PHENIX software suite (27). Elements of rRNA or r-proteins present in the atomic model of the 50S subunit absent from the cryo-EM maps were removed from the final models. The final models obtained for the $44S_{R3C}$ class 1 and $44S_{R70P}$ class 1 were validated using Phenix cryo-EM Comprehensive validation tool and the Molprobity server (28,29) (Supplementary Tables S2).

Figures were prepared using UCSF Chimera (20) and Chimera X (21,22) and Photoshop (Adobe).

RESULTS

Cryo-EM structure of the 44S assembly intermediates.

The two 44S particles we chose to analyze from the spontaneous suppressor collection of mutants of the RbgA-F6A strain were the $44S_{R3C}$ particles from the R3C strain (RB1055) and $44S_{R70P}$ particles from the R70P strain (RB1051) (10). These strains express uL6 either with an Arginine 3 to Cysteine (R3C) or an Arginine 70 to Proline (R70P) single point mutations. Quantitative mass spectrometry (qMS) analysis revealed that the $44S_{R3C}$ and $44S_{R70P}$ particles had an $uL6_{R3C}$ and $uL6_{R70P}$ occupancy of 0.8 and <0.2, respectively. The uL6 occupancy in the $45S_{RbgA}$ particles was 1 (4). The protein complement for all other r-proteins was similar in the two 44S particles and to the $45S_{RbgA}$ particle. They contained most of the r-proteins at stoichiometric levels, except for uL16, bL28, bL35 and bL36 that were severely depleted, and bL27, bL31 and bL33 that were partially depleted and showed an occupancy ranging from 0.5 to 0.7. No peptides for uL11 were detected in any of the particles (Supplementary Figure S1 and Supplementary Table S1). These results indicate that our purification approach rendered $44S_{R3C}$ and $44S_{R70P}$ particles with a protein complement consistent with previous analysis of these particles (3,4,10).

To investigate why the $45S_{RbgA}$ particle is entirely dependent on RbgA for assembly, whereas the 44S particles can mature in the presence of a functionally compromised RbgA variant, we determined the cryo-EM structure of the $44S_{R3C}$ and $44S_{R70P}$ particles. We found that both the $44S_{R3C}$ and $44S_{R70P}$ particles co-existed as two classes (classes 1 and 2) (Supplementary Figures S2 and S4). Both classes were equally populated in the case of the $44S_{R70P}$ particles (Supplementary Figure S4), but class 1 was more abundant in the $44S_{R3C}$ sample (Supplementary Figure S3). The cryo-EM map for each class (Figure 1) was refined to a resolution of ∼3 Å (Supplementary Figures S3 and S5). Two features were constant in all the obtained classes (Figure 2): (i) the body region adopted the mature conformation, and (ii) most of the rRNA helices in the A, P and E functional sites were still in an immature conformation. Neither map showed densities representing rRNA helices H38, H89, H91 and H92 in the A site, H69, H71 and H93 in the P site and H68 in the E site. The L1 stalk comprised of helices H76-78 was also not visible in any of the structures, as most of the densities representing helices H42-44 forming the L7/12 stalk and GAC (Figure 2A,B; Videos 1 and 2). The differential feature between classes 1 and 2 was the CP. Class 1 in both the $44S_{R3C}$ and $44S_{R70P}$ particles showed partial density for H80-88 and 5S rRNA forming the CP. However, class 2 in both types of particles showed no density for any of the CP components (Figure 2A,B; Videos 1 and 2).

Consistent with the qMS results, we did not find density in any of the cryo-EM maps for several r-proteins located at the base of the CP, including uL11, uL16, bL27, bL28, bL31, bL33, bL35 and bL36. Density for uL6, which was present at an occupancy of 0.8 and < 0.2 in the $44S_{R3C}$ and $44S_{R70P}$ populations, respectively, was also not apparent in any of the maps (Supplementary Figure S6). This result suggested that $uL6_{R3C}$ variant, when present, is bound in a flexible manner. Similarly, three other proteins, uL5, uL10 in the CP and uL18 in the L7/12 stalk, were also bound in a flexible way and did not appear in the maps, even though qMS data indicated they were present at an occupancy of 1.

Overall, the cryo-EM structures obtained for classes 1 and 2 of the $44S_{R3C}$ and $44S_{R70P}$ particles resemble the structure of the $45S_{RbgA}$ particle (Figure 2C) (5) with densities missing for the same rRNA helices and r-proteins. However, the one notable difference was rRNA helices H42-44. In the $45S_{RbgA}$ particle, these helices are ordered, and C1095 and A1096 in H42 interact through H-bonding and base stacking with G2780 in H97. This interaction stabilizes H42 and H97 into a rigid conformation (Figure 3A). Instead, in classes 1 and 2 obtained for the $44S_{R3C}$ (Figure 3B) and $44S_{R70P}$ (Figure 3C) particles, H42 remains in a flexible conformation, and a stable interaction between H42 with H97 is not observed. Consequently, the cryo-EM densities associated with helices H42 with H97 are highly fragmented.

Furthermore, temperature maps obtained by comparing molecular models of the $44S_{R3C}$ (class 1) and $44S_{R70P}$ (class 1) particles (Supplementary Table S2) with the mature 50S subunit revealed that H42 with H97 and the binding site for uL6 adopts a more immature conformation in the 44S particles than in the $45S_{RbgA}$ particle (Supplementary Figure S7).

Because the main compositional difference between the $45S_{RbgA}$ particle and the $44S_{R3C}$ and $44S_{R70P}$ particles is the r-protein uL6, these results indicate that when wild-type uL6 is present in the particle in full occupancy, it locks H97, H42 and the surrounding region into a defined conformation similar to that in the mature 50S subunit. This conformation is not induced by the $uL6_{R3C}$ variant, which binds the 44S particles with lower occupancy or the $uL6_{R70P}$ variant, which is not incorporated into the $44S_{R70P}$ particles (Supplementary Figure S1). Consequently, H42 in the $44S_{R3C}$ and $44S_{R70P}$ particles remained in a flexible conformation.

The 44S particles mature through alternative maturation pathways

To visualize how the $44S_{R3C}$ and $44S_{R70P}$ particles evolve into mature subunits, we took purified 44S particles and exposed them for 15 min at 37°C to RbgA in a buffer containing GMPPNP. We then visualized these *in vitro* matured particles by cryo-EM.

In the experiment performed with the $44S_{R3C}$ particles, we found all the subunits underwent maturation and appeared to exist in two subpopulations, classes 1 and 2, which contained 70% and 30% of the particles, respectively (Supplementary Figure S8). The cryo-EM maps for these two classes (Figure 4A,B; left panels) were refined to 2.8 and 2.9Å resolution (Supplementary Figure S9). Contrary to the untreated $44S_{R3C}$ particles (Figures 1 and 2), the two classes showed most of the rRNA helices in the A, P and E functional sites in a mature conformation. Only H38 and H89 in the A side and most of H69 in the P site remained highly flexible and invisible in the cryo-EM maps (Figure 4A,B, middle panels; Video 3). The main difference between the two classes was the existence of an almost fully assembled CP in class 1, but the lack of it in class 2 (Figure 4A,B, middle panels; Video 3). In both classes, we found that despite the extensive maturation that the functional core exhibited, a stable interaction between H42 with H97 was not observed. Densities representing most of these two helices were missing (Figure 4A,B; right panels).

In the parallel experiment performed with $44S_{R70P}$ particles, we found that after exposure to RbgA, two classes of particles (classes 1 and 3) (Supplementary Figure S10) were at the same maturation state as those found in the experiment with the $44S_{R3C}$ particles (Figure 5A,C, top panels, Video 4). The cryo-EM maps for these two classes were refined to 3.1 and 3.2 Å resolution, respectively (Supplementary Figure S11). These classes also exhibited most of the rRNA helices in the functional sites in a mature conformation, except for H38 and H89 in the A side and H69 in the P site, which were invisible (Figure 5A,C, middle panels; Video 4). The CP in class 3 was also immature, as was the case for class 2 in the experiment with the $44S_{R3C}$ particles. These two classes attracted most of the particles in the dataset (54% and a 23%, respectively). In addition, we also found that 9% (class 2) and 10% of the particles (class 4) in the dataset (Supplementary Figure S10) did not un-

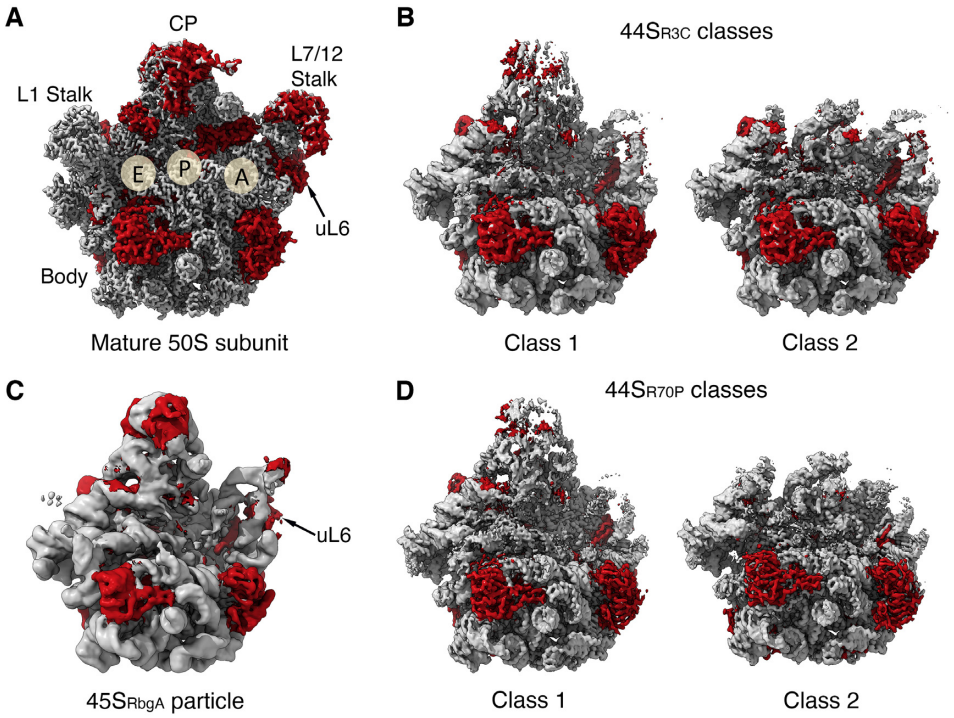

Figure 1. Cryo-EM structure of the $44S_{R3C}$ and $44S_{R70P}$ particles. (**A**) The structure of the mature 50S subunit from *B. subtilis* is shown to highlight the main landmarks in the ribosomal subunit, including the A, P and E functional sites. The rRNA is shown in gray, and the r-proteins are shown in red. The location of r-protein uL6 is indicated. This map was obtained by applying a low pass filter of 4 Å to the molecular model of the 50S subunit from *B. subtilis* (PDB ID: 3j9w) (18). (**B**) Cryo-EM maps obtained for classes 1 and 2 of the $44S_{R3C}$ particles. (**C**) The cryo-EM map of the $45S_{RbgA}$ particle (5) is shown in this panel for comparative purposes. (**D**) Cryo-EM maps obtained for classes 1 and 2 of the $44S_{R70P}$ particles. All maps displayed are unsharpened.

dergo any apparent maturation (Figures 5B,D) and were virtually identical to the classes 1 and 2 found for the untreated $44S_{R70}$ particles (Figures 1D and 2B). These two classes showed most of the rRNA helices in the A, P and E functional sites in an immature state. Class 4 also lacked the CP. The maps for classes 2 and 4 refined to 3.5 and 4.1 Å resolution, respectively (Supplementary Figure S11). None of these four classes displayed a stable interaction between H97 and H42, and density was lacking for most of these two rRNA helices (Figure 5, bottom panels). Finally, 4% of the observed particles represented 70S ribosomes likely formed by association of class 1 $44S_{R70}$ particles with contaminating 30S particles existing in the fractions of the sucrose gradient that contained the $44S_{R70}$ particles.

Previous work analyzing the RbgA-induced maturation of the $45S_{RbgA}$ particle (5) found that maturation of the CP is essential for the functional sites of the 50S subunit to mature. Unlike the $45S_{RbgA}$ particle, the $44S_{R3C}$ and $44S_{R70P}$ particles could mature most of the rRNA helices in the functional sites without first forming the CP (Figures 4 and 5). Consequently, we concluded that the $44S_{R3C}$ and $44S_{R70P}$ particles assembled in the presence of RbgA follow a different maturation pathway than the $45S_{RbgA}$ particles. Because the only structural difference existing between the $45S_{RbgA}$ particle and the 44S particles is in H97 and H42, the new structures suggest that the lack of a defined conformation for these two helices provides the 44S particles with the ability to mature through alternative assembly pathways.

The 44S particles maintain the ability to bind RbgA and RbgA-F6A

An intriguing result from our cryo-EM analysis of the *in vitro* maturation reactions of RbgA-treated $44S_{R3C}$ and $44S_{R70P}$ particles was that none of the obtained classes showed a density attached to the P-site that could be assigned to RbgA (Figure 4C). To test whether the particles retained the ability to bind RbgA, we determined the dissociation constant (K_d value) of each 44S particle from RbgA using microscale thermophoresis (MST). In these assays, the thermophoretic mobility of fluorescently labeled RbgA was measured at increasing concentration of each of the 44S particles. We found that RbgA had K_d values of 98 ± 2 nM and 145 ± 3 nM with respect to the $44S_{R3C}$ and $44S_{R70P}$ particles, respectively (Supplementary Figure S12A). These affinity measurements were comparable to the K_d values of RbgA to the $45S_{RbgA}$ particle (93 ± 3 nM) that is known to interact with RbgA (5,7).

The $44S_{R3C}$ and $44S_{R70P}$ particles also maintained their ability to bind the GTPase deficient RbgA-F6A variant but with lower affinity. The RbgA-F6A variant showed K_d values of 377 ± 8 nM and 215 ± 2 nM with respect to the $44S_{R3C}$ and $44S_{R70P}$ particles, respectively (Supplementary Figure S12B). This was important as the 44S particle evolves into mature 50S subunits in the presence of the RbgA-F6A variant in the suppressor strains where these intermediates accumulate.

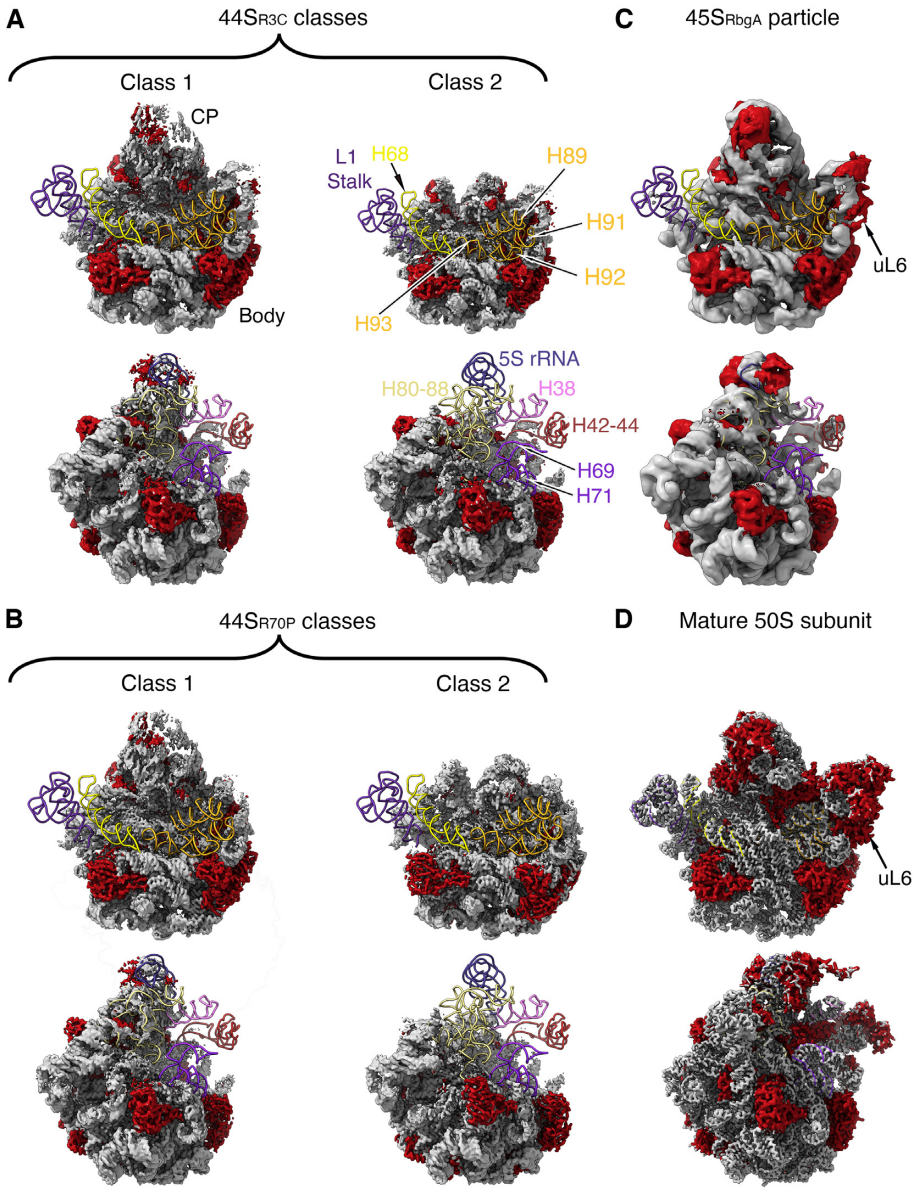

Figure 2. Multiple rRNA helices remain in an immature state in the $44S_{R3C}$ and $44S_{R70P}$ particles. (**A**) The rRNA helices not represented by density in the cryo-EM maps obtained for the $44S_{R3C}$ particle classes 1 and 2 are shown in various colors. Helices contiguous within the primary sequence are given the same color. The color code is maintained for all the panels across the figure. For a better visibility, two different views are shown for each class. The 'crown' view (top panels) shows missing helices H89 and H91-92 in the A site, H93 in the P site and H68 in the E site. Helices forming the L1 stalk are also shown in this view. The oblique view (bottom panels) shows H80-88 and 5S rRNA, comprising the central protuberance (CP). This view also shows H69 and H71 in the P site and H42-44 that are part of L7/L12 stalk. The rRNA helices shown in various colors are from the molecular model of the 50S subunit from *B. subtilis* (PDB ID: 3j9w) (18). In the cryo-EM maps the rRNA is shown in gray, and the r-proteins are shown in red. (**B**) Equivalent views as shown in panel A for the cryo-EM structures of classes 1 and 2 obtained for the $44S_{R70P}$ particle. (**C**) Crown and oblique views showing the rRNA helices missing in the $45S_{RbgA}$ particle (5) and in (**D**) the 50S mature subunit. This map was obtained by applying a low pass filter of 4 Å to the molecular model of the 50S subunit from *B. subtilis* (PDB ID: 3j9w). The location of r-protein uL6 visible in the $45S_{RbgA}$ particle and mature 50S subunit is indicated. All maps displayed in (A–C) are unsharpened. The $45S_{RbgA}$ particle and 50S mature subunit are shown for comparison purposes.

Therefore, these experiments suggested that the 44S particles retained their ability to bind RbgA and the RbgA-F6A variant. The absence of RbgA in our cryo-EM structures may have been caused by RbgA being released once the 44S particles underwent the described maturation steps or the factor having fallen off upon exposure to the water–air interface during cryo-EM grid preparation.

Dependency on RbgA for in vitro maturation of the 44S particles.

To test whether the 44S particles can mature *in vitro* in a reaction without added RbgA, we took purified total ribosomal particles from the RB1055 (R3C) and RB1051 (R70P) strains and incubated them at 37°C for 15 min in the presence or absence of 40-fold excess of RbgA. Control reac-

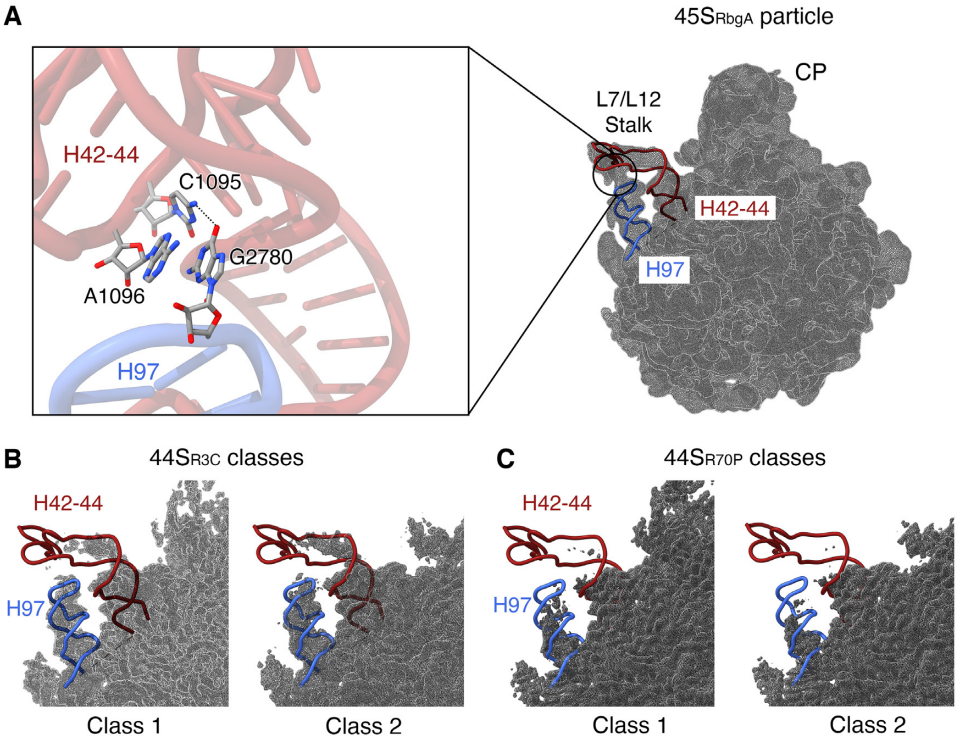

Figure 3. Helices 42 and 97 in the 23S rRNA maintain a flexible conformation in the $44S_{R3C}$ and $44S_{R70P}$ particles. (**A**) Cryo-EM density map of the $45S_{RbgA}$ particle (5) with the docked molecular model for helices 42 and 97 (right panel). In the $45S_{RbgA}$ particle, both rRNA helices form a H-bonding and base stacking stabilizing interaction involving nucleotides C1095 and A1096 in H42 and G2780 in H97 (left panel). (**B**) Zoom-in view of the H42 and H97 region of the cryo-EM maps obtained for the $44S_{R3C}$ classes 1 and 2 shows that the density for H42-44 is highly fragmented and the stabilizing interaction with H97, existing in the $45S_{RbgA}$ particle is lacking in these structures. (**C**) An equivalent view of the cryo-EM maps obtained for the $44S_{R70P}$ classes 1 and 2 shows the lack of a stabilizing interaction between H42 and H97. All maps shown in this figure are unsharpened.

tions were carried out in parallel by incubating them at 4°C for 15 min. All reactions contained 2 mM GMPPNP. Once incubations were completed, ribosomal particles in each reaction were separated using sucrose gradient centrifugation, and we used the increased proportion of 70S ribosomes in the ribosome profiles to gage the fraction of 44S particles that had evolved into mature 50S subunits and associated with existing 30S subunits (Supplementary Figure S13A).

We found that in reactions containing ribosomal particles from the RB1055 strain where we added RbgA, many of the $44S_{R3C}$ particles matured and assembled into 70S ribosomes (Supplementary Figure S13B). However, maturation of the $44S_{R3C}$ particles and the appearance of 70S ribosomes did not occur in the absence of RbgA. Surprisingly, reactions assembled with ribosomal particles from the RB1051 strain showed maturation of the $44S_{R70P}$ particles and association into 70S ribosomes only in the reaction without added RbgA (Supplementary Figure S13C). Because our cryo-EM experiments had shown clear maturation of the $44S_{R70P}$ particles in *in vitro* reactions with RbgA treatment (Figure 4 and 5), we rationalized that RbgA remained bound to the $44S_{R70P}$ particles that had matured and prevented their association into 70S ribosomes. To test this possibility, we repeated the reactions for this sample but only added a 5-fold molar excess of RbgA and replaced the GMPPNP nucleotide in the reaction by 2 mM GTP (Supplementary Figure S13D). In this case, both the reaction with and without RbgA treatment showed an increase in the 70S fraction, indicating that the $44S_{R70P}$ particle matured in an *in vitro* reaction without added RbgA. None of the control reactions maintained at 4°C for 15 min showed a significant 70S fraction in their ribosome profiles.

The main compositional and structural difference between the $44S_{R3C}$ and $44S_{R70P}$ particles is their uL6 content. The $44S_{R3C}$ particle contains the $uL6_{R3C}$ variant at high occupancy, and the $44S_{R70P}$ particles is almost entirely depleted from $uL6_{R70P}$. Therefore, these results suggest that the complete loss of uL6 enables the $44S_{R70P}$ particle to mature without adding RbgA in the reaction.

RbgA-independent maturation of the $44S_{R70P}$ particles occurs through alternative maturation pathways.

To investigate whether the maturation experienced by the $44S_{R70P}$ particles in a reaction without RbgA is similar to that observed in the reaction containing RbgA, we took purified $44S_{R70P}$ particles and checked by western blot that residual amounts of RbgA-F6A protein did not copurify with the ribosomal particles (Supplementary Figure S14). We found this to be the case, and we then incubated these $44S_{R70P}$ particles for 15 min at 37°C without RbgA, before visualizing them by cryo-EM.

Three-dimensional classification of the cryo-EM images showed the particles co-existed in three classes (Supplementary Figure S15 and Figure 6, top panels) that refined to ∼3.3 Å resolution (Supplementary Figure S16). Classes 1 and 3 were particles with mature functional sites (Fig-

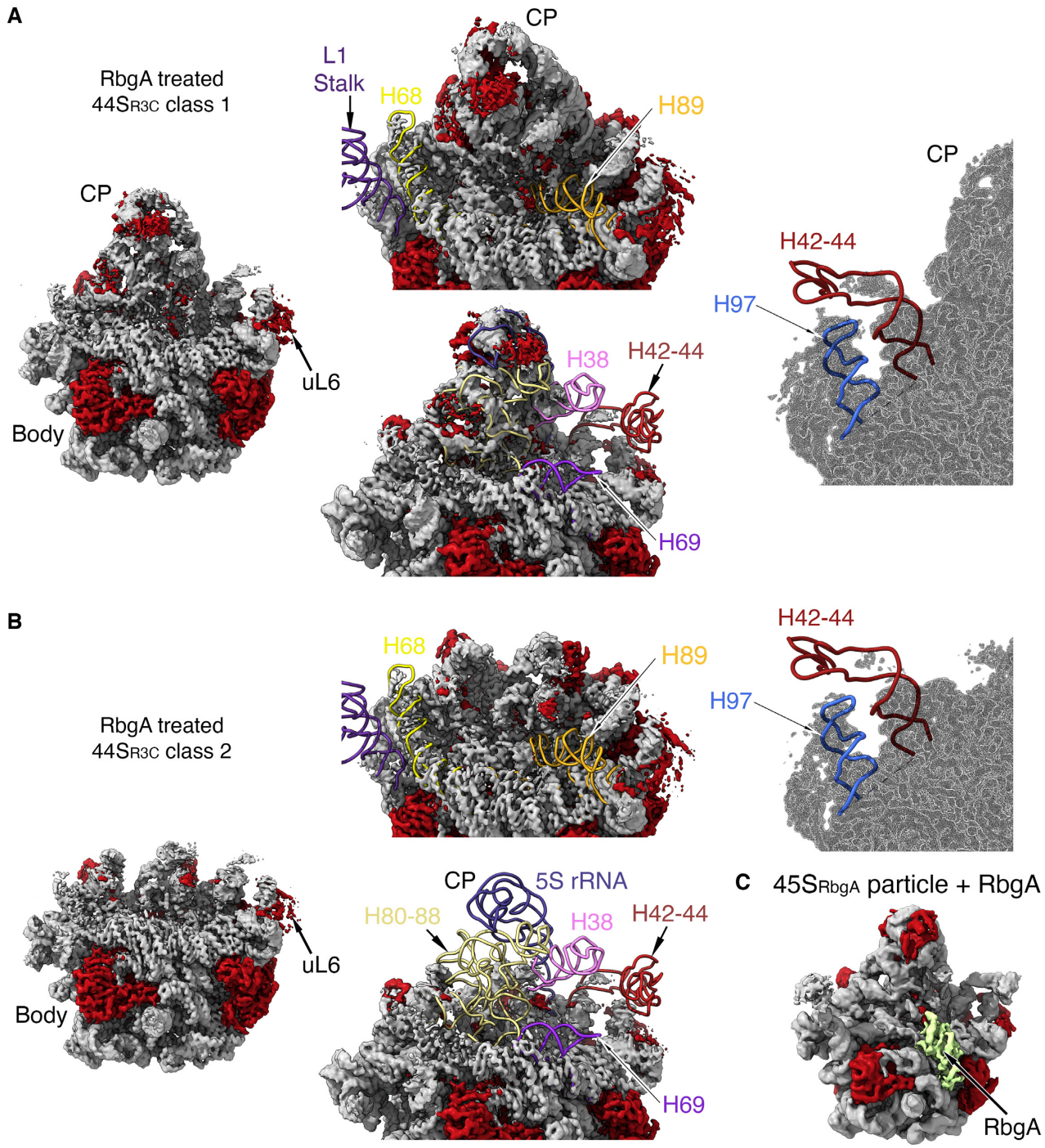

Figure 4. Cryo-EM analysis of RbgA treated $44S_{R3C}$ particle. (**A**) Purified $44S_{R3C}$ particles were incubated with RbgA at 37ºC for 15 min before imaging them by cryo-EM. The left panel shows the cryo-EM map of the $44S_{R3C}$ particle class 1. The middle panel shows a zoomed image of the crown view and an oblique view of the particle, labeling those rRNA helices for which density is missing or fragmented. The molecular model for the missing rRNA helices was obtained by docking the molecular model of the 50S subunit from *B. subtilis* (PDB ID: 3j9w) (18) into the cryo-EM map. The right panel shows a close-up view of the H42 and H97 region of the cryo-EM map revealing that a stable interaction between these two rRNA motifs is still lacking. (**B**) Panels are arranged similarly to (A) show the structural details of the $44S_{R3C}$ particle class 2. The rRNA is shown in gray in the cryo-EM maps, and the r-proteins are shown in red. (**C**) Cryo-EM structure of the $45S_{RbgA}$ particle bound to RbgA. Produced from EMDB ID 20441. All maps shown in this figure are unsharpened.

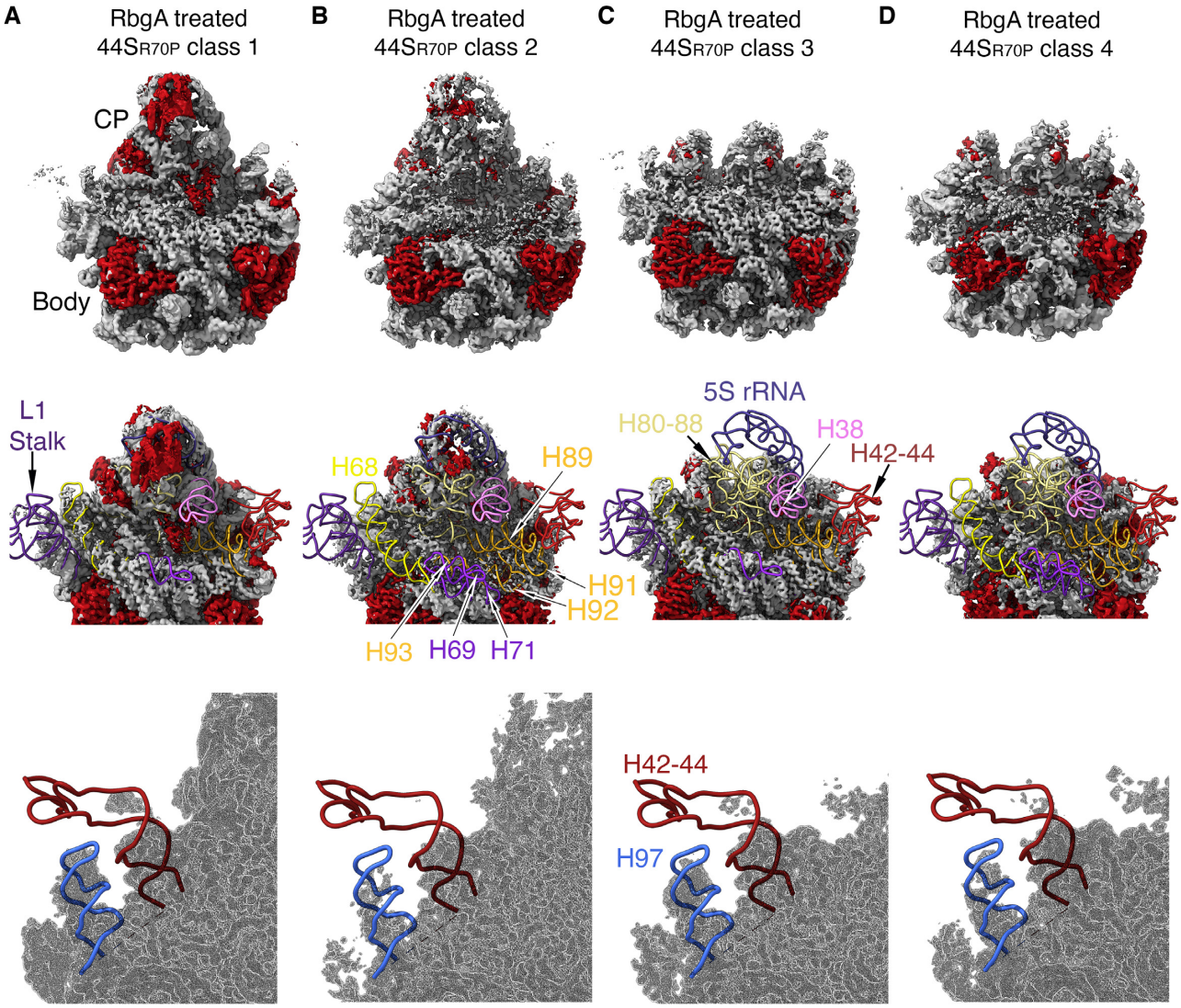

Figure 5. Cryo-EM analysis of RbgA treated $44S_{R70P}$ particle. Purified $44S_{R70P}$ particles were incubated with RbgA at 37°C for 15 min and imaged by cryo-EM. (**A–D**) The top panels show the cryo-EM map of the $44S_{R70P}$ particle classes 1 to 4. The panels below show zoomed images of the crown view of the cryo-EM maps with rRNA helices for which density is missing, shown as a ribbon representation. Color coding of these helices is maintained across the entire figure. The molecular model for the missing rRNA helices was obtained by docking the molecular model of the 50S subunit from *B. subtilis* (PDB ID: 3j9w) (18) into the cryo-EM map. Close-up views of the H42 and H97 region of the cryo-EM maps for classes 1 to 4 are shown in the bottom panel. The molecular models of the two helices are docked into the cryo-EM maps. A stable interaction between H42 and H97 is not present in any of the classes. The rRNA is shown in grey in the cryo-EM maps, and the r-proteins are shown in red. All maps shown in this figure are unsharpened.

ure 6A,C, top panel; video 5). H91 and H92 in the A site, H71 and H93 in the P showed a mature conformation. H68 in the E site showed a fragmented density. H89 and H38 in the A site and most of H69 in the P site were still invisible in these two classes. Class 1 also had a formed CP, but this motif was absent in class 3 (Figure 6A,C, middle panel; video 5). These two classes represented 23% and 14% of the particles from the dataset, respectively (Supplementary Figure S15). Class 2 showed a completely immature functional core (Figure 6B, middle panel). None of the three classes showed H97 and H42 in a mature conformation (Figure 6, bottom panels).

To ensure the observed RbgA-independent maturation of the $44S_{R70P}$ particles in our *in vitro* maturation assay was happening exclusively with these particles, we repeated the experiment with purified $45S_{RbgA}$ particles, which are known to require RbgA for maturation (4,5). The purified $45S_{RbgA}$ particles were analyzed by western blot to rule out that RbgA did not co-purify in these samples (Supplementary Figure S14). Subsequently, the $45S_{RbgA}$ particles were incubated for 15 min at 37°C, before visualizing them by cryo-EM. We found the same two assembly intermediates that appeared with unincubated $45S_{RbgA}$ particles (5) (Supplementary Figure S17). The two classes were refined to ∼3 Å resolution (Supplementary Figure S18). Both classes 1 and 2 presented the rRNA helices in the A, P and E functional sites still in an immature conformation. Class 2 was also missing all the densities for the CP. Both classes showed H42 and H97 forming the stabilizing interaction (Supplementary Figure S19).

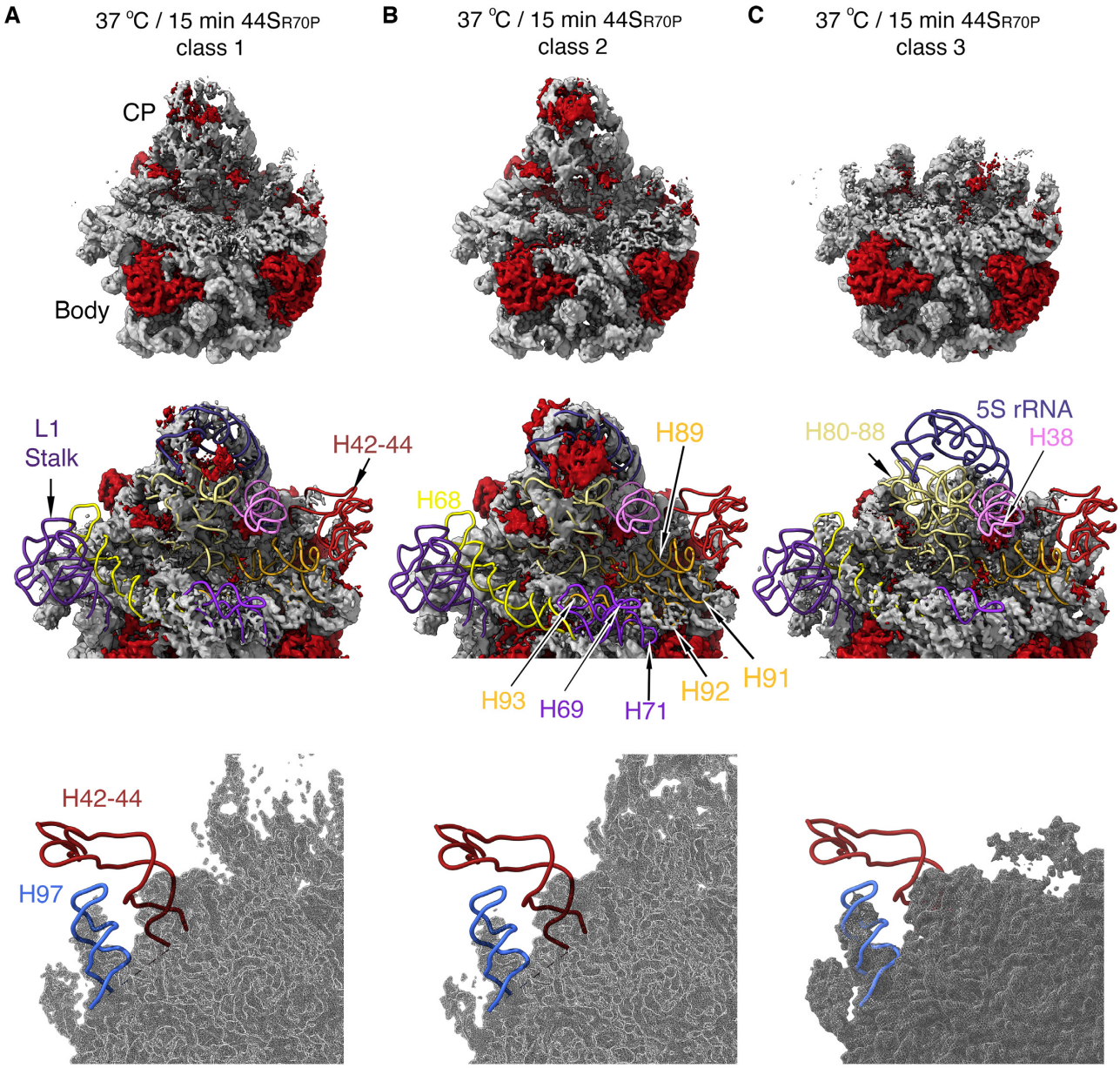

Figure 6. RbgA-independent maturation of the $44S_{R70P}$ particle visualized by cryo-EM. Purified $44S_{R70P}$ particles were incubated for 15 min at 37°C before visualizing them by cryo-EM. (**A–C**) Image classification revealed the existence of three classes in this sample. The cryo-EM maps for classes 1 to 3 are shown on the top panels. Middle panels highlight those rRNA helices in the structures lacking or having fragmented density. The molecular model for the missing rRNA helices was obtained by docking the molecular model of the 50S subunit from *B. subtilis* (PDB ID: 3j9w) (18) into the cryo-EM map. The bottom panels show zoomed views of the H42 and H97 regions with the molecular model for these two helices docked into the cryo-EM map. The two helices remain in non-stable conformation after the incubation treatment. The rRNA is shown in gray in the cryo-EM maps, and the r-proteins are shown in red. All maps shown in this figure are unsharpened.

Therefore, we concluded that the $44S_{R70P}$ particles mature *in vitro* independently from RbgA following the same alternative maturation pathways to those exhibited by these particles in the presence of RbgA.

The 70S ribosomes in the suppressor strains present a mature GTPase-associated center (GAC)

Finally, we obtained the cryo-EM structure of the 70S ribosomes from the RB1051 (R70P) strain. Classification analysis of the cryo-EM particles produced only one class (Supplementary Figure S20) that refined to 2.8 Å (Supplementary Figure S21). The cryo-EM map for this class (Supplementary Figure S22A) revealed densities corresponding for the $uL6_{R70P}$ variant expressed by this suppressor strain and also for all other late entry r-proteins depleted in the $44S_{R70P}$ particles, including uL16 (Supplementary Figure S22B), which is incorporated only at the end of the maturation process (4,8,9). More importantly, H97 and H42 formed a stable interaction in these 70S ribosomes, and the GAC was fully assembled (Supplementary Figure S22C). These results were consistent with previous qMS analysis

(10), showing that the 70S ribosomes assembled in the suppressor strains had a complete protein complement.

Overall, these results suggest that even though the 44S particles mature following non-canonical pathways, they are incorporated into structurally complete 70S ribosomes.

DISCUSSION

Understanding the essential role of RbgA in the maturation of the 50S subunit

To understand what step during the large subunit assembly makes RbgA an essential factor, we purified 44S particles from the R3C ($44S_{R3C}$) and R70P ($44S_{R70P}$) RbgA suppressor strains. Each one of these strains expresses the RbgA-F6A variant, which exhibits significantly reduced GTPase activity and an uL6 variant. The uL6 variant incorporated into these particles contains either a R3C or R70P single point mutation in the N-terminal region of the r-protein (10). These strains were chosen because under our purification conditions, these 44S particles showed the most dissimilar uL6 content, with an occupancy of ~0.8 in the $44S_{R3C}$ particles and of <0.2 in the $44S_{R70P}$ particles (Supplementary Figure S1). Biochemical and cryo-EM analysis of the purified $44S_{R3C}$ and $44S_{R70P}$ particles found that incorporating these uL6 variants into the 44S assembly intermediates caused H42 and H97 to remain in a flexible conformation.

Instead, incorporation of a copy of wild-type uL6 in the $45S_{RbgA}$ particle before the CP is formed stabilizes H42 and H97 into a defined conformation and pauses the maturation of the A, P and E sites until RbgA acts. RbgA only recognizes the $45S_{RbgA}$ particle once the CP has been formed. Upon binding in their P site, RbgA licenses further folding of the functional sites (5). By this mechanism, RbgA ensures that the maturation of the functional sites occurs last and only after the CP has been formed (Figure 7A). Instead, the $44S_{R3C}$ and $44S_{R70P}$ particles containing a flexible H42:H97 structural motif can take alternative folding pathways. In this case, the presence of an already formed CP is no longer a prerequisite for the maturation of the functional sites (Figure 7B).

The dependence on RbgA for these alternative folding pathways is less than for the canonical pathway. The ability of the $44S_{R3C}$ and $44S_{R70P}$ particles to mature *in vitro* independently of RbgA inversely correlated with their uL6 occupancy (Supplementary Figure S1). The $44S_{R3C}$ particles containing $uL6_{R3C}$ at 0.8 occupancy still require RbgA in the reaction to mature through the alternative folding pathways. However, $44S_{R70P}$ particles, which are primarily $uL6_{R70P}$ depleted, continue their assembly in a reaction without RbgA (Figure 6).

These results reveal that the binding of uL6 locks the conformation of H97 and H42 and, in turn, pauses the maturation of the A, P and E sites of the assembling subunit into the conformation observed in the $45S_{RbgA}$ particle. However, these particles move forward in the maturation process by assembling the CP. RbgA is an essential factor in *B. subtilis* because it is required by the $45S_{RbgA}$ particle containing a CP to continue the assembly steps involving the maturation of the A, P and E sites (Figure 7A). By making the maturation of the functional sites dependent on RbgA binding, and RbgA being only able to recognize $45S_{RbgA}$ particles that contain a formed CP, *B. subtilis* cells ensure that the ribosomal particle first mature the CP and only then the maturation of the A, P and E site proceeds (Figure 7A).

Integration of YphC and YsxC in the RbgA-catalyzed maturation of the 50S subunit functional sites.

In addition to RbgA, YphC and YsxC are also two essential GTPases that assist in the late stages of assembly of the 50S subunit. Like the RbgA depletion strain, YphC and YsxC depleted strains accumulate immature 50S subunits, named $45S_{YphC}$ and $44.5S_{YsxC}$ particles (30). These ribosomal particles are identical in protein complement and remarkably similar in structure to the $45S_{RbgA}$ particles. More importantly, uL6 is contained at high occupancy, and their H42 and H97 form the same stabilizing interaction involving nucleotides C1095 and A1096 and G2780 that we observed in the $45S_{RbgA}$ particles (7). An interesting property shared by the $45S_{RbgA}$, $45S_{YphC}$ and $44.5S_{YsxC}$ particles is that they are promiscuous, and every particle can bind individually each of the GTPases. Simultaneous binding of RbgA, YphC and YsxC to each of these assembly intermediates is also possible (7).

These properties of the $45S_{RbgA}$, $45S_{YphC}$ and $44.5S_{YsxC}$ particles, along with our new results, allow us to extend our model for how the late stages of maturation of the 50S subunit occur involving RbgA, YphC and YsxC and explain the reason behind their essentiality. As described, binding of uL6 during 50S subunit assembly pauses the maturation process into the conformation represented by the $45S_{RbgA}$, $45S_{YphC}$ and $44.5S_{YsxC}$ particles. Assembling particles arrive at this conformation already containing a CP and likely through multiple assembly pathways. RbgA, YphC and YsxC bind to this stage and work in conjunction to complete the maturation of the functional sites. Whether binding occurs simultaneously or sequentially is still unknown, but existing data suggest that a specific binding hierarchy does not exist (7). The binding of these factors licenses the A, P and E sites to continue their maturation.

RbgA, in particular, triggers the maturation of rRNA helices H91-92 and H38 in the A site and H93 in the P site (5). The exact role of YphC and YsxC is still uncharacterized, but these two factors likely assist the folding of the other rRNA helices in which RbgA does not participate, including the long helix H68 in the E site, H89 in the A site and folding of H69 and H71 in the P site. The three factors may also assist in the recruitment and stabilization of the r-proteins that are still missing from the $45S_{RbgA}$, $45S_{YphC}$ and $44.5S_{YsxC}$ particles. The observed binding promiscuity of the YphC, YsxC and RbgA GTPases and the fact that a specific binding hierarchy does not likely exist allows for these last steps of the assembly of the 50S subunit involving the maturation of the A, P and E sites to occur without following a precise sequence.

Other bacterial species also ensure the functional sites in the 50S subunit assemble last through uncharacterized RbgA-independent mechanisms.

Why did *B. subtilis* evolve to dedicate at least three assembly factors to ensure the maturation of the A, P and E sites occurs last? One reason is that maintaining the functional sites

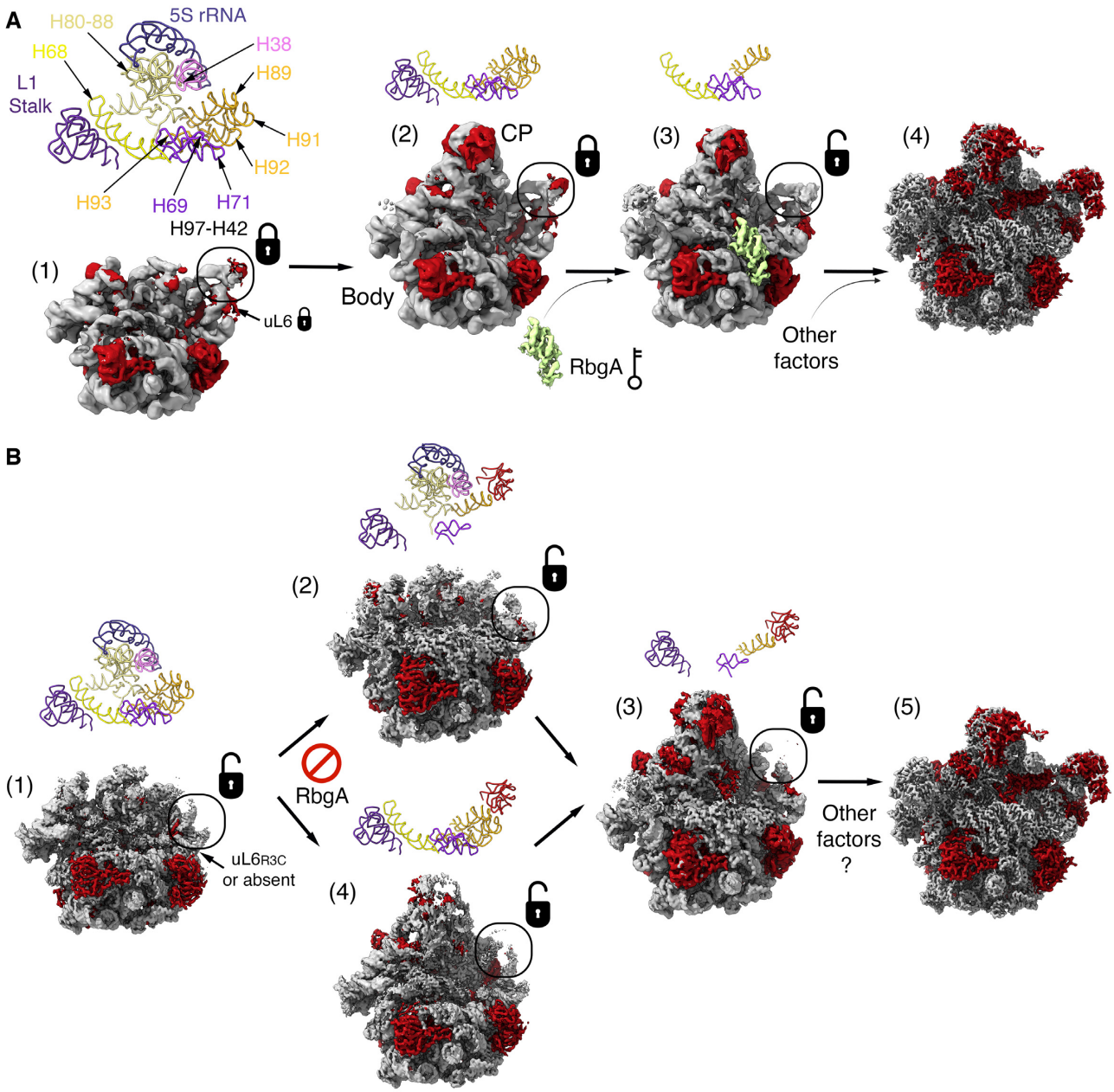

Figure 7. Proposed model for the essential role of RbgA in the maturation of the 50S subunit. (**A**) Canonical pathway for the assembly of the 50S subunit. The binding of uL6 to the assembling ribosomal particle stabilizes the interaction of H42 and H97, locking the structure and pausing the maturation of the rRNA helices in the A, P and E functional sites (1). The assembling particle continues to mature by folding the rRNA helices integrating the CP (2). The particle containing the CP is recognized by RbgA, which binds to the P site, as a key that unlocks the structure (3). This unlocked structure continuous to mature the A, P and E functional sites in steps mediated by RbgA and possibly by other additional assembly factors (4). The rRNA and r-proteins in the cryo-EM maps are colored in gray and red, respectively. The diagram on top of each cryo-EM structure shows the rRNA helices that remain unfolded at each stage. rRNA helices are labeled in (1), and color code is maintained throughout the figure. (**B**) In the suppressor strains, the uL6 R3C r-protein variant associates with the assembling particle. However, differently from the parental strain, this variant does not stabilize the interaction of H42 and H97 in the $44S_{R3C}$ particle. The uL6 R70P variant does not bind to the $44S_{R70P}$ particles, and their H42 and H97 also remain in a non-stable conformation (1). Consequently, the structure remains unlocked and free to mature either the functional sites first (2) and CP second (3) or in reverse order (4 and 3). The RbgA-dependency for these maturation steps in the $44S_{R3C}$ particle is less than in the $45S_{RbgA}$ particle, and it does not require RbgA at all in the case of the $44S_{R70P}$ particles. Whether other assembly factors are required for the $44S_{R3C}$ and $44S_{R70P}$ particles to reach the mature state (5) is still unknown.

of the 45S particles in an immature state until all other structural motifs are formed prevents the premature association of the assembling subunits with 30S subunits and becoming prematurely engaged in translation. It is also possible that the canonical assembly pathway in which the CP is formed ahead of the functional sites (Figure 7A) represents a more efficient maturation pathway. It is plausible that the alternative pathway exhibited by the $44S_{R3C}$ and $44S_{R70P}$ particles where folding of the CP precedes or is simultaneous to the folding of the A, P and E sites (Figure 7B) may have a higher frequency of generating dead-end intermediates that must be cleared by ribosome degradation pathways.

Data are still insufficient to understand this aspect of the 50S subunit assembly pathway fully. Nevertheless, other bacterial species which do not contain the *rbgA* gene in their genome have also adopted RbgA-independent mechanisms to ensure the maturation of the CP also precedes the assembly of the functional sites. A recent study (31) performed an *in vitro* reconstitution of *E. coli* 50S ribosomal subunits from purified components and in the complete absence of assembly factors. *E. coli* is one of the bacterial species lacking RbgA. Time course cryo-EM analysis of the assembly reactions identified a total of five distinct precursors of the 50S subunit. These assembly intermediates defined a progressive maturation pathway consistent with the 'canonical' pathway described here (Figure 7A), with maturation of the CP preceeding maturation of the functional sites. Interestingly, none of the identified assembly intermediates in the study exhibited H42 and H97 in the stable conformation described for the *B. subtilis* 45S structures. Consistently, uL6 in all these maps exhibited a fragmented density. However, maturation in the observed intermediates still occurs through the canonical pathway. These results suggest that in *E. coli,* the ribosomal components by themselves can ensure that the A, P and E sites mature last. The existence of bacterial species in which the canonical pathway is encoded in the actual ribosomal components underscores the importance of the correct timing for folding the functional sites in the 50S subunit.

In a different study, Davis *et al.* (32) analyzed by qMS and cryo-EM the 50S assembly intermediates that appear upon depletion of bL17 in *E. coli*. The absence of bL17 also prevents the incorporation of bL32 into the large subunit (33). These two proteins are situated at a strategically significant position in the core of the large subunit. Accordingly, the absence of these two r-proteins renders the core of the subunit unstable, provoking the accumulation of some additional intermediates exhibiting various structural defects in this region independently of the maturation state of the CP and A, P and E functional sites. The 13 precursors described in this work (32) were organized within three parallel routes that ultimately merged into a still immature 50S subunit. Nevertheless, these three pathways completely agreed with the canonical pathway of assembly described here (Figure 7A).

Overall, the results presented here explain the functional interplay between uL6 and the ribosomal assembly factor RbgA to ensure the assembly of critical functional motifs of the 50S subunit in *B. subtilis* follows a specifically defined sequence of events.

DATA AVAILABILITY

The cryo-EM maps obtained in this study and the model for the $44S_{R3C}$ class 1 and $44S_{R70P}$ class 1 have been deposited in the Electron Microscopy Data Bank (EMDB) and the Protein Data Bank (PDB) with accession codes detailed in Supplementary Tables S2–S5.

The mass spectrometry proteomics data have been deposited to the ProteomeXchange Consortium via the PRIDE (34) partner repository with the dataset identifier PXD023644.

SUPPLEMENTARY DATA

Supplementary Data are available at NAR Online.

ACKNOWLEDGEMENTS

We thank K. Sears, M. Strauss and other staff members of the Facility for Electron Microscopy Research (FEMR) at McGill University for help with microscope operation and data collection. Titan Krios cryo-EM data were collected at FEMR (McGill).

FUNDING

Canadian Institutes of Health Research [PJT-153044 to J.O.]; NIH [R01GM110248 to R.A.B. Funding for open access charge: Canadian Foundation for Innovation.
Conflict of interest statement. The authors declare no competing financial interests. The funders had no role in study design, data collection and analysis, decision to publish or manuscript preparation.

REFERENCES

1. Morimoto,T., Loh,P.C., Hirai,T., Asai,K., Kobayashi,K., Moriya,S. and Ogasawara,N. (2002) Six GTP-binding proteins of the era/obg family are essential for cell growth in bacillus subtilis. *Microbiology*, **148**, 3539–3552.
2. Uicker,W.C., Schaefer,L. and Britton,R.A. (2006) The essential GTPase RbgA (YlqF) is required for 50S ribosome assembly in bacillus subtilis. *Mol. Microbiol.*, **59**, 528–540.
3. Li,N., Chen,Y., Guo,Q., Zhang,Y., Yuan,Y., Ma,C., Deng,H., Lei,J. and Gao,N. (2013) Cryo-EM structures of the late-stage assembly intermediates of the bacterial 50S ribosomal subunit. *Nucleic Acids Res.*, **41**, 7073–7083.
4. Jomaa,A., Jain,N., Davis,J.H., Williamson,J.R., Britton,R.A. and Ortega,J. (2014) Functional domains of the 50S subunit mature late in the assembly process. *Nucleic Acids Res.*, **42**, 3419–3435.
5. Seffouh,A., Jain,N., Jahagirdar,D., Basu,K., Razi,A., Ni,X., Guarne,A., Britton,R.A. and Ortega,J. (2019) Structural consequences of the interaction of RbgA with a 50S ribosomal subunit assembly intermediate. *Nucleic Acids Res.*, **47**, 10414–10425.
6. Ban,N., Beckmann,R., Cate,J.H., Dinman,J.D., Dragon,F., Ellis,S.R., Lafontaine,D.L., Lindahl,L., Liljas,A., Lipton,J.M. *et al.* (2014) A new system for naming ribosomal proteins. *Curr. Opin. Struct. Biol.*, **24**, 165–169.
7. Ni,X., Davis,J.H., Jain,N., Razi,A., Benlekbir,S., McArthur,A.G., Rubinstein,J.L., Britton,R.A., Williamson,J.R. and Ortega,J. (2016) YphC and YsxC GTPases assist the maturation of the central protuberance, GTPase associated region and functional core of the 50S ribosomal subunit. *Nucleic Acids Res.*, **44**, 8442–8455.
8. Teraoka,H. and Nierhaus,K.H. (1978) Protein L16 induces a conformational change when incorporated into a L16-deficient core derived from Escherichia coli ribosomes. *FEBS Lett.*, **88**, 223–226.

9. Kazemie,M. (1975) The importance of Escherichia coli ribosomal proteins L1, L11 and L16 for the association of ribosomal subunits and the formation of the 70-S initiation complex. *Eur. J. Biochem.*, **58**, 501–510.
10. Gulati,M., Jain,N., Davis,J.H., Williamson,J.R. and Britton,R.A. (2014) Functional interaction between ribosomal protein L6 and RbgA during ribosome assembly. *PLos Genet.*, **10**, e1004694.
11. Schroeder,J.W. and Simmons,L.A. (2013) Complete genome sequence of bacillus subtilis strain PY79. *Genome Announc.*, **1**, e01085-13.
12. Gulati,M., Jain,N., Anand,B., Prakash,B. and Britton,R.A. (2013) Mutational analysis of the ribosome assembly GTPase RbgA provides insight into ribosome interaction and ribosome-stimulated GTPase activation. *Nucleic Acids Res.*, **41**, 3217–3227.
13. Martin,L.B., Sherwood,R.W., Nicklay,J.J., Yang,Y., Muratore-Schroeder,T.L., Anderson,E.T., Thannhauser,T.W., Rose,J.K. and Zhang,S. (2016) Application of wide selected-ion monitoring data-independent acquisition to identify tomato fruit proteins regulated by the CUTIN DEFICIENT2 transcription factor. *Proteomics*, **16**, 2081–2094.
14. Schorb,M., Haberbosch,I., Hagen,W.J.H., Schwab,Y. and Mastronarde,D.N. (2019) Software tools for automated transmission electron microscopy. *Nat. Methods*, **16**, 471–477.
15. Zheng,S.Q., Palovcak,E., Armache,J.P., Verba,K.A., Cheng,Y. and Agard,D.A. (2017) MotionCor2: anisotropic correction of beam-induced motion for improved cryo-electron microscopy. *Nat. Methods*, **14**, 331–332.
16. Zivanov,J., Nakane,T., Forsberg,B.O., Kimanius,D., Hagen,W.J., Lindahl,E. and Scheres,S.H. (2018) New tools for automated high-resolution cryo-EM structure determination in RELION-3. *eLife*, **7**, e42166.
17. Zhang,K. (2016) Gctf: Real-time CTF determination and correction. *J. Struct. Biol.*, **193**, 1–12.
18. Sohmen,D., Chiba,S., Shimokawa-Chiba,N., Innis,C.A., Berninghausen,O., Beckmann,R., Ito,K. and Wilson,D.N. (2015) Structure of the bacillus subtilis 70S ribosome reveals the basis for species-specific stalling. *Nat. Commun.*, **6**, 6941.
19. de la Rosa-Trevin,J.M., Oton,J., Marabini,R., Zaldivar,A., Vargas,J., Carazo,J.M. and Sorzano,C.O. (2013) Xmipp 3.0: an improved software suite for image processing in electron microscopy. *J. Struct. Biol.*, **184**, 321–328.
20. Pettersen,E.F., Goddard,T.D., Huang,C.C., Couch,G.S., Greenblatt,D.M., Meng,E.C. and Ferrin,T.E. (2004) UCSF Chimera–a visualization system for exploratory research and analysis. *J. Comput. Chem.*, **25**, 1605–1612.
21. Goddard,T.D., Huang,C.C., Meng,E.C., Pettersen,E.F., Couch,G.S., Morris,J.H. and Ferrin,T.E. (2018) UCSF chimerax: meeting modern challenges in visualization and analysis. *Protein Sci.*, **27**, 14–25.
22. Pettersen,E.F., Goddard,T.D., Huang,C.C., Meng,E.C., Couch,G.S., Croll,T.I., Morris,J.H. and Ferrin,T.E. (2021) UCSF chimerax: structure visualization for researchers, educators, and developers. *Protein Sci.*, **30**, 70–82.
23. Afonine,P.V., Poon,B.K., Read,R.J., Sobolev,O.V., Terwilliger,T.C., Urzhumtsev,A. and Adams,P.D. (2018) Real-space refinement in PHENIX for cryo-EM and crystallography. *Acta Crystallogr. D Struct. Biol.*, **74**, 531–544.
24. Emsley,P. and Cowtan,K. (2004) Coot: model-building tools for molecular graphics. *Acta Crystallogr. D Biol. Crystallogr.*, **60**, 2126–2132.
25. Emsley,P., Lohkamp,B., Scott,W.G. and Cowtan,K. (2010) Features and development of coot. *Acta Crystallogr. D Biol. Crystallogr.*, **66**, 486–501.
26. Terwilliger,T.C., Sobolev,O.V., Afonine,P.V. and Adams,P.D. (2018) Automated map sharpening by maximization of detail and connectivity. *Acta Crystallogr. D Struct. Biol.*, **74**, 545–559.
27. Adams,P.D., Afonine,P.V., Bunkoczi,G., Chen,V.B., Davis,I.W., Echols,N., Headd,J.J., Hung,L.W., Kapral,G.J., Grosse-Kunstleve,R.W. *et al.* (2010) PHENIX: a comprehensive Python-based system for macromolecular structure solution. *Acta Crystallogr. D Biol. Crystallogr.*, **66**, 213–221.
28. Afonine,P.V., Klaholz,B.P., Moriarty,N.W., Poon,B.K., Sobolev,O.V., Terwilliger,T.C., Adams,P.D. and Urzhumtsev,A. (2018) New tools for the analysis and validation of cryo-EM maps and atomic models. *Acta Crystallogr. D Struct. Biol.*, **74**, 814–840.
29. Williams,C.J., Headd,J.J., Moriarty,N.W., Prisant,M.G., Videau,L.L., Deis,L.N., Verma,V., Keedy,D.A., Hintze,B.J., Chen,V.B. *et al.* (2018) MolProbity: more and better reference data for improved all-atom structure validation. *Protein Sci.*, **27**, 293–315.
30. Schaefer,L., Uicker,W.C., Wicker-Planquart,C., Foucher,A.E., Jault,J.M. and Britton,R.A. (2006) Multiple GTPases participate in the assembly of the large ribosomal subunit in bacillus subtilis. *J. Bacteriol.*, **188**, 8252–8258.
31. Nikolay,R., Hilal,T., Qin,B., Mielke,T., Burger,J., Loerke,J., Textoris-Taube,K., Nierhaus,K.H. and Spahn,C.M.T. (2018) Structural visualization of the formation and activation of the 50S ribosomal subunit during in vitro reconstitution. *Mol. Cell*, **70**, 881–893.
32. Davis,J.H., Tan,Y.Z., Carragher,B., Potter,C.S., Lyumkis,D. and Williamson,J.R. (2016) Modular assembly of the bacterial large ribosomal subunit. *Cell*, **167**, 1610–1622.
33. Herold,M. and Nierhaus,K.H. (1987) Incorporation of six additional proteins to complete the assembly map of the 50 s subunit from escherichia coli ribosomes. *J. Biol. Chem.*, **262**, 8826–8833.
34. Perez-Riverol,Y., Csordas,A., Bai,J., Bernal-Llinares,M., Hewapathirana,S., Kundu,D.J., Inuganti,A., Griss,J., Mayer,G., Eisenacher,M. *et al.* (2019) The PRIDE database and related tools and resources in 2019: improving support for quantification data. *Nucleic Acids Res.*, **47**, D442–D450.